Daily mitochondrial dynamics in cone photoreceptors

Michelle M. Giarmarco[a], Daniel C. Brock[a], Brian M. Robbings[a], Whitney M. Cleghorn[a], Kristine A. Tsantilas[a], Kellie C. Kuch[a], William Ge[a], Kaitlyn M. Rutter[a], Edward D. Parker[b], James B. Hurley[a,b], and Susan E. Brockerhoff[a,b,1]

[a]Department of Biochemistry, University of Washington, Seattle, WA 98195; and [b]Department of Ophthalmology, University of Washington, Seattle, WA 98195

Edited by Jeremy Nathans, Johns Hopkins University School of Medicine, Baltimore, MD, and approved October 2, 2020 (received for review April 24, 2020)

Cone photoreceptors in the retina are exposed to intense daylight and have higher energy demands in darkness. Cones produce energy using a large cluster of mitochondria. Mitochondria are susceptible to oxidative damage, and healthy mitochondrial populations are maintained by regular turnover. Daily cycles of light exposure and energy consumption suggest that mitochondrial turnover is important for cone health. We investigated the three-dimensional (3D) ultrastructure and metabolic function of zebrafish cone mitochondria throughout the day. At night retinas undergo a mitochondrial biogenesis event, corresponding to an increase in the number of smaller, simpler mitochondria and increased metabolic activity in cones. In the daytime, endoplasmic reticula (ER) and autophagosomes associate more with mitochondria, and mitochondrial size distribution across the cluster changes. We also report dense material shared between cone mitochondria that is extruded from the cell at night, sometimes forming extracellular structures. Our findings reveal an elaborate set of daily changes to cone mitochondrial structure and function.

photoreceptors | zebrafish | retina | mitochondria | circadian

Photoreceptor cells in the retina are highly metabolically active. Their energy demands change throughout the day to support phototransduction (1) and regeneration of outer segment (OS) disks (2). Photoreceptors consume more energy as ATP in darkness than in light (1) and some additional ATP comes from mitochondrial metabolism (3).

Energy production can be influenced by mitochondrial fission, fusion, and new growth (mitogenesis). Smaller, fragmented mitochondria typically consume less oxygen (4). Mitogenesis is influenced by many factors, including circadian rhythms (5). In neurons mitogenesis can occur far away from the cell body (6). Mitochondria can form networks (7) and folds of cristae within mitochondria can be remodeled (8). These dynamic processes contribute to cell health; mitochondrial dysfunction is associated with neurodegenerative diseases (9–11), including retinal degeneration (12, 13).

Over 90% of glucose taken up by photoreceptors is used for aerobic glycolysis (14, 15). Nevertheless, they have a large cluster of mitochondria in the apical portion of the inner segment, the ellipsoid, just below the OS. The density and organization of mitochondrial clusters vary among species, but they are present in photoreceptors of all vertebrates examined, including fish (16), ground squirrels (17), mice (18), and humans (19). In photoreceptors of some species, all mitochondria reside within the cluster, while in mammals with vascularized inner retinas mitochondria are also present at synaptic terminals (20, 21). In cultured chicken retinas, mitochondrial dynamics are circadian (22), but diurnal changes in mitochondrial structure and function in photoreceptors in intact eyes have not been explored. Daily exposure to sometimes intense light and high rates of energy production suggest that mitochondrial turnover may be important for photoreceptor health. Structural and functional changes to mitochondria could enable photoreceptors to meet increased ATP requirements in darkness.

In this report we describe daily changes that occur in zebrafish cone photoreceptor mitochondria. Zebrafish provide a useful model to dissect mitochondrial dynamics in specific photoreceptor subclasses. Zebrafish undergo typical vertebrate behavioral and biological circadian rhythms (23, 24), and their retinas have four cone subtypes (red, green, blue, and ultraviolet [UV]) organized in a tiered, mosaic pattern. Each cone type can be identified by its unique morphology and position in the outer retina (25), and each maintains a large cluster of mitochondria just below the OS (16). Our results indicate that mitochondrial clusters in cones undergo diurnal remodeling consistent with enhanced energy production in darkness.

Results

To examine mitochondrial cluster function and dynamics throughout the day, we collected retinas at six timepoints from adult zebrafish under 14-h/10-h light-dark (LD) or 24-h dark (DD) conditions. Retinas were used for imaging and biochemical experiments. Fig. 1*A* illustrates individual cone cell structures with immunohistochemistry (IHC) and electron microscopy (EM). Cone subtypes were differentiated by double cone position, nuclear morphology, and presence of a distinct large mitochondrion at the base of UV cone clusters (Fig. 1*A*, white arrows). At night zebrafish cone ellipsoids and OSs extend distally into the retinal pigment epithelium (RPE); in the morning they retract back toward the nuclear layer (*SI Appendix*, Fig. S1*A*). This daily process of retinomotor movements is regulated by light exposure and the circadian clock (26, 27).

Significance

Mitochondria are organelles that make cellular energy. In the retina, mitochondrial health is important for photoreceptor cell function and normal vision. Photoreceptors need more energy at night, but it is unclear how their mitochondria adapt to changing energy demands. We investigated zebrafish cone photoreceptor mitochondria throughout the day. At night cone mitochondria are smaller, more numerous, and more metabolically active. Material from mitochondria is also released from photoreceptors during nighttime, forming stalks and networks outside of the cell. In daytime, photoreceptor mitochondria associate with ER and autophagosomes, organelles that mediate mitochondrial turnover. These daily changes to mitochondrial structure may help photoreceptors adapt to metabolic demands of daytime and nighttime.

Author contributions: M.M.G., D.C.B., K.A.T., E.D.P., J.B.H., and S.E.B. designed research; M.M.G., D.C.B., B.M.R., W.M.C., K.A.T., K.C.K., W.G., and E.D.P. performed research; M.M.G., D.C.B., B.M.R., W.M.C., K.C.K., W.G., K.M.R., J.B.H., and S.E.B. analyzed data; and M.M.G., D.C.B., J.B.H., and S.E.B. wrote the paper.

The authors declare no competing interest.

This article is a PNAS Direct Submission.

[1]To whom correspondence may be addressed. Email: sbrocker@uw.edu.

This article contains supporting information online at https://www.pnas.org/lookup/suppl/doi:10.1073/pnas.2007827117/-/DCSupplemental.

First published November 3, 2020.

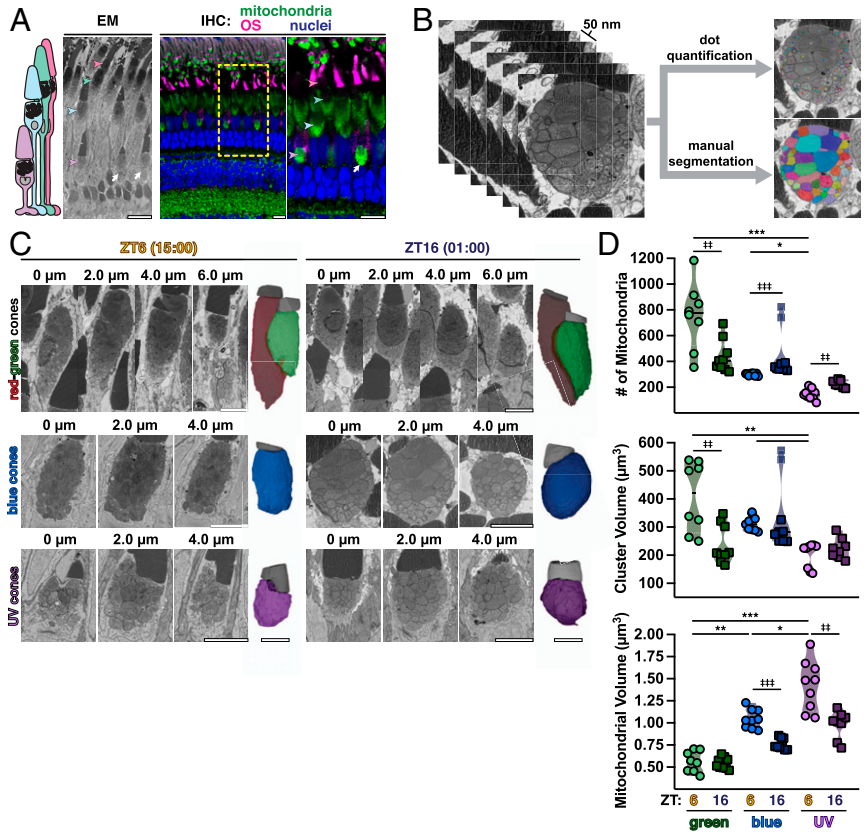

Fig. 1. At night single cones have more small mitochondria. (*A*) Schematic of zebrafish cone subtypes (*Left*), with EM (*Middle*) and IHC (*Right*) images of zebrafish outer retina. IHC images are stained for all mitochondria (green), red-green cone OSs (magenta), and nuclei (blue). Arrowheads indicate corresponding UV, blue, green, and red cone mitochondrial clusters; white arrows, megamitochondria at UV cluster bases. Yellow box, zoomed-in area. (Scale bars, 10 µm.) (*B*) Example 50-nm Z-stack from SBFSEM used for 3D analysis via manual segmentation or rapid dot quantification. (*C*) Z-stacks from SBFSEM with 3D-rendered mitochondrial clusters (colored) and OSs (gray) from green, blue, and UV cone subtypes in daytime at ZT6 (15:00) and night at ZT16 (01:00). (Scale bars, 5 µm.) (*D*) Violin plots of mitochondrial number, cluster volume, and mitochondrial volume from dot quantification and manual segmentation; lines represent median. Cone subtypes are represented by respective colors at ZT6 (circles) and ZT16 (squares). *,‡$P < 0.05$. **, ‡‡$P < 0.01$. ***,‡‡‡$P < 0.001$. *SI Appendix*, Table S2 lists statistical information and Ns from each group.

Zebrafish Single Cones Have More Small Mitochondria at Night. We performed detailed three-dimensional (3D) analyses of cone mitochondrial clusters using 50 nm Z-sections collected by serial block-face scanning electron microscopy (SBFSEM) (Fig. 1*B* and Movie S1). Image stacks were analyzed using either a rapid dot quantification method or manual segmentation to compare mitochondrial number, size, shape, and location between day (15:00, Zeitgeber Time 6 [ZT6]) and night (01:00, ZT16). Individual red-green, blue, and UV cone image stacks with corresponding 3D renderings of mitochondrial clusters and OSs at ZT6 and ZT16 are presented in Fig. 1*C*. *SI Appendix*, Fig. S2 presents 3D renderings with mitochondrial numbers and cluster volumes for all cells in this study.

We found that at night, blue and UV cone mitochondria increase in number by 17 ± 10% and 57 ± 6%, respectively (Fig. 1 *D*, *Top*). These changes did not coincide with an increase in cluster volume (Fig. 1 *D*, *Middle*); on average, volumes of individual blue and UV cone mitochondria decreased at night by 29 ± 3% and 31 ± 6%, respectively (Fig. 1 *D*, *Bottom*). One animal in the study (*SI Appendix*, Fig. S2, fish 7) had overall larger cones than all others, and its blue cones were identified as outliers using a robust regression followed by outlier identification test (transparent markers at ZT16 in Fig. 1*D*). For transparency we included these two cones in the analysis, but this did not affect the conclusions. Green cones, which in zebrafish exist in red-green double cones, appeared in two populations at both timepoints. Four animals in our study have very large green cones (>700 mitochondria), while the green cones of four other animals are smaller (300 to 450 mitochondria) (Fig. 1*D* and *SI Appendix*, Fig. S2). Despite this bimodal population, mitochondrial volume for green cones is maintained between 0.4 and 0.7 µm^3 at ZT6 and ZT16. This suggests that single and double cone subtypes undergo different cycles of mitochondrial dynamics.

Mitochondrial cluster shape was also examined for each cone subtype using transgenic zebrafish expressing YFP targeted to cone mitochondria (gnat2:mito-cpYFP) (28), counterstained with antibodies targeting components of the mitochondrial respiratory chain (*SI Appendix*, Fig. S1*A* and Table S1 lists antibodies used). Individual cone mitochondrial cluster lengths and circularity ratios were calculated. For all cone types, cluster length increases at night by ~50% (*SI Appendix*, Fig. S1 *B*, *Top*), but cluster width, reflected by the circularity ratio, decreases at this time (*SI Appendix*, Fig. S1 *B*, *Bottom*). Both LD and DD groups exhibited cyclical changes in cluster morphology.

Cone Mitochondria within Clusters Vary in Size and Complexity. Surface area and volume of each manually segmented mitochondrion was used to calculate mitochondrial complexity index (MCI), a size-insensitive measure of morphological complexity (29). Mitochondria within clusters were heterogeneous in volume and MCI (Fig. 2*A*), and MCI was poorly correlated with volume (Fig. 2*B*). Four individual mitochondria with the same volume but different

MCIs are presented in Fig. 2*C*. Compared to mouse cones, zebrafish cone mitochondria are simpler on average but occupy a larger volume (*SI Appendix*, Fig. S3).

Mitochondria in Cone Subtypes Are Morphologically Distinct, and More Simple Mitochondria Appear at Night. Our analyses also revealed morphological distinctions between cone subtypes. Clusters in green cones are longer (*SI Appendix*, Figs. S1*C* and S2) and have smaller mitochondria (Fig. 1*D*). Fig. 2*D* and Movie S2 depict 3D renderings of manually segmented green, blue, and UV cone clusters. At ZT6, green, blue, and UV mitochondria have significantly different distributions of mitochondrial volume, with mitochondrial volumes largest in UV cones and smallest in green cones, but cone subtypes do not have significantly different MCI distributions (Fig. 2*E*).

To compare mitochondrial volume and MCI between day and night, we analyzed manually segmented green, blue, and UV

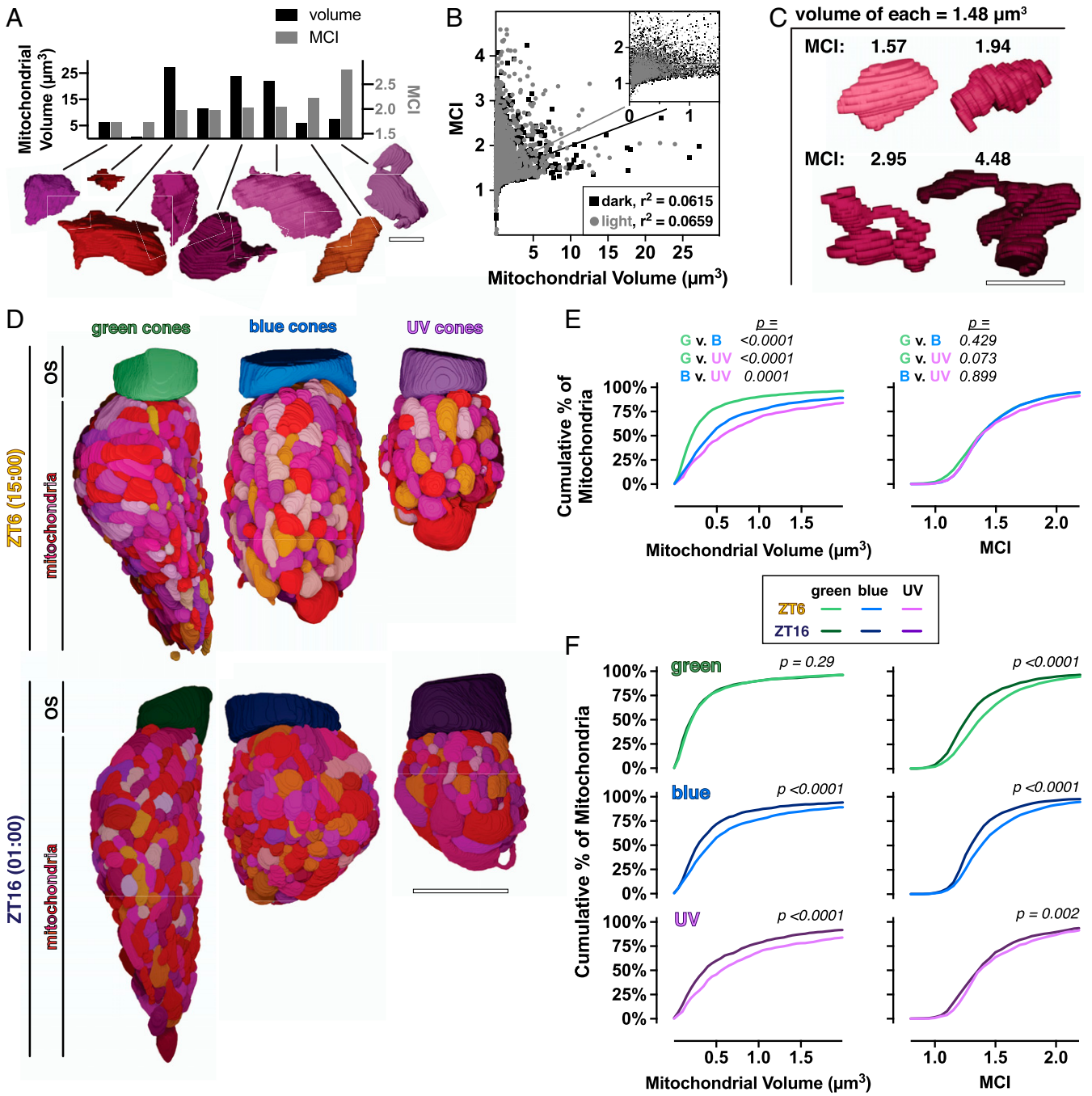

Fig. 2. At night cones have more simple mitochondria. (*A*) Three-dimensional renderings of eight manually segmented cone mitochondria with corresponding quantifications of volume (*Left* axis, black bars) and MCI (*Right* axis, gray bars). (Scale bar, 2 μm.) (*B*) Cross-correlation plot of mitochondrial volume and MCI for individual mitochondria at ZT16 (black squares) and ZT6 (gray circles). (*C*) Three-dimensional renderings of single mitochondria with equal volumes (1.48 μm^3) over a range of MCIs. (Scale bar, 2 μm.) (*D*) Three-dimensional renderings from manual segmentation of mitochondria and OSs in green, blue, and UV cones at ZT6 and ZT16. (Scale bar, 5 μm.) (*E*) Cumulative frequency distributions for mitochondrial volume and MCI comparing mitochondria between cone subtypes at ZT6. (*F*) Cumulative frequency distributions for cone subtypes, comparing mitochondrial volume and MCI at ZT6 (light lines) and ZT16 (dark lines). ZT6 curves are also presented in *E*; *SI Appendix*, Table S2 lists Ns from all groups.

cones at ZT6 and ZT16. At ZT16, mitochondria are significantly smaller in blue and UV cones, but not green cones (Fig. 2*F*). The MCI of all cone subtypes shifts significantly toward having more simple mitochondria at night. These results suggest that green cones can alter their mitochondrial complexity without changing volume.

Megamitochondria Associate in the Cluster Core. Cones of several species (30–32), including zebrafish (33), contain large megamitochondria. To examine the distribution of megamitochondria in zebrafish cone clusters, we 3D rendered the three largest mitochondria in manually segmented cones in their respective clusters. In all cone subtypes, megamitochondria localize within the cluster core, often in direct contact (Fig. 3*A*). We did not detect striking differences in megamitochondria between day and night, but note that the volume, location, and complexity of megamitochondria vary between cone subtypes (*SI Appendix*, Fig. S4). Megamitochondria in green cones localize to the top of the cluster and are relatively uniform in size and of average complexity. Single cones contain distinct megamitochondria whose volume comprises 12 to 22% of the cluster. We observed several megamitochondria with projections extending toward the cluster periphery, and UV cone megamitochondria are unusually complex.

Mitochondria in the Cluster Core Are Smaller at Night. To examine the distribution of mitochondrial sizes across the cluster, each mitochondrion from SBFSEM analyses was plotted as a single point in 3D using its center X-Y-Z coordinates (Fig. 3*B*). For manual segmentation, point size was proportional to mitochondrial volume. For dot quantification, point size was proportional to the number of dots needed to track each mitochondrion; larger points represent larger or more branched mitochondria. Points were separated into peripheral and core populations according to distance from the cluster 3D central axis. Similarly, top and bottom populations were defined by proximity to the OS or cluster base. Mitochondrial point sizes were quantified in relation to cluster position (Fig. 3*C*), and ratios of core/periphery and top/bottom were used to assay relative size distribution (Fig. 3*D*).

At ZT6, cones have significantly more large mitochondria at the cluster core, compared to the periphery (Fig. 3 *C* and *D*, *Left*). At ZT16 average mitochondrial point size decreases 30 to 45% in the core and ∼30% in the periphery; size also decreases ∼35 to 50% at the bottom of the cluster (Fig. 3*C*). Conceptually, this represents a shift toward more small mitochondria at the base of the cluster at night (Fig. 3*D*). Compared to single cones, green cones underwent similar changes to mitochondrial size distribution, but maintain a significantly larger population of small mitochondria at the cluster base (Fig. 3 *D*, *Right*). These data suggest that in daytime all cones maintain a population of small mitochondria at the cluster periphery; at night mitochondrial size becomes more uniform across the cluster.

Endoplasmic Reticulum–Mitochondrial Appositions Peak in Daytime. In other cells the organelle endoplasmic reticulum (ER) initiates mitochondrial fission (34, 35), a process that occurs at the end of mitogenesis (36). Zebrafish cone ER primarily contacts mitochondria at the cluster base and periphery (28), where mitochondrial size is most dynamic. We examined the cone ER network surrounding mitochondria at all timepoints. Using sections from LD or DD transgenic zebrafish expressing GFP targeted to cone ER (gnat2:er-GFP) (37), we performed IHC with antibodies against the mitochondrial respiratory chain (Fig. 3*E*). To quantify potential ER contacts for individual blue and UV cone clusters, ER–mitochondrial apposition ratios were calculated by dividing the longest length of ER adjacent to the cluster by the cluster length.

In the daytime, ER tightly associates with the entire cluster surface and is densely packed around its base (Fig. 3 *E*, *Top*). At night, apposition ratios decrease as the ER becomes more diffuse and extends less toward the OS (Fig. 3 *E*, *Bottom* and Fig. 3*F*). This shows that the ER network changes to accommodate the mitochondrial cluster and is consistent with the shift toward larger mitochondria at the top and periphery of single cone clusters at night (Fig. 3*D*). At most timepoints ER–mitochondrial apposition ratios are lower for the DD group (Fig. 3*F*), suggesting that light exposure drives tighter ER–mitochondrial associations.

Mitogenesis Genes Peak before Night Onset. Increased mitogenesis could result in more cone mitochondria at night. Mitogenesis is controlled at the transcriptional level (38, 39): upstream signals lead to mitochondrial DNA (mtDNA) replication, protein synthesis, and fission creating new mitochondria (Fig. 4*A*). We measured mRNA transcript levels of mitogenesis genes using qPCR with whole retinas (40) (*SI Appendix*, Table S3 lists primers; *SI Appendix*, Table S4 lists fitting parameters for cosinor curves). The early nuclear transcription factors *pgc1α* and *pgc1β* rise in the morning, while the mitochondrial transcription factor *tfam*, DNA polymerase *polg1*, and deacetylase *sirt3* all peak before night onset (Fig. 4*B*). Together this suggests that canonical mitogenesis increases at night in whole retinas.

Transcripts encoding the mitochondrial fusion protein *mfn2* rise in the morning (Fig. 4 *C*, *Top*), suggesting fusion could mediate the corresponding decrease in mitochondrial number in cones; a recent study found that cones contribute roughly half of the mitochondrial proteins in adult zebrafish retina (41). No significant changes were detected in the zebrafish cone mitochondrial enlarging factor *es1* (42) (Fig. 4 *C*, *Middle*). As a control we examined *aanat2* (43), which displays robust circadian changes in expression (Fig. 4 *C*, *Bottom*). Transcript levels between LD and DD groups were similar, and *tfam*, *polg1*, and *sirt3* met statistical cutoffs for rhythmicity, indicating that retinal expression of mitogenesis genes is regulated primarily by the circadian clock.

Mitochondrial-Associated Autophagosomes Peak in Daytime. A selective form of autophagy called mitophagy clears damaged or unnecessary mitochondria (44). While several pathways can trigger mitophagy (45, 46), all coalesce on recruitment of LC3 to maturing mito-autophagosomes. We performed IHC at all timepoints using LD or DD transgenic zebrafish expressing GFP fused to LC3 in cones (gnat2:GFP-LC3) (37) and antibodies against the mitochondrial respiratory chain (Fig. 4*D*). LC3-positive autophagosomes overlapping with blue and UV cone mitochondrial clusters were quantified. The number of mitochondrial-associated autophagosomes increases twofold at light onset (Fig. 4*E*). While changes to autophagosome numbers met statistical cutoffs for circadian rhythmicity, more mitochondrial-associated autophagosomes were present in the DD group in the evening, possibly indicative of enhanced mitochondrial turnover in prolonged darkness.

When viewed using EM, autophagosomes appear as lucent, multivesicular structures (Fig. 4 *F*, *Left*, yellow arrowheads), while mitochondria are electron dense and contain cristae folds. We validated our IHC findings by quantifying the number of electron-lucent structures in all cone mitochondrial clusters imaged using SBFSEM. More lucent structures are present in clusters at ZT6 (Fig. 4 *F*, *Right*), when more mitochondrial-associated autophagosomes were detected using IHC. Several clusters contain >30 lucent structures in the daytime, suggestive of a mitophagic event at this timepoint.

Cone Mitochondria Mislocalize toward the Cell Body Hours before Light Onset. Degraded mitochondrial material canonically enters the endolysosomal pathway (45), but in neurons it can translocate and leave the cell (47, 48). Mitochondria mislocalize toward the nucleus in degenerating human cones (12) and in a zebrafish cone model of mitochondrial calcium overload (41). Four hours before light onset (05:00, ZT20), we observed mislocalized cone mitochondria using IHC with gnat2:mito-cpYFP transgenic zebrafish

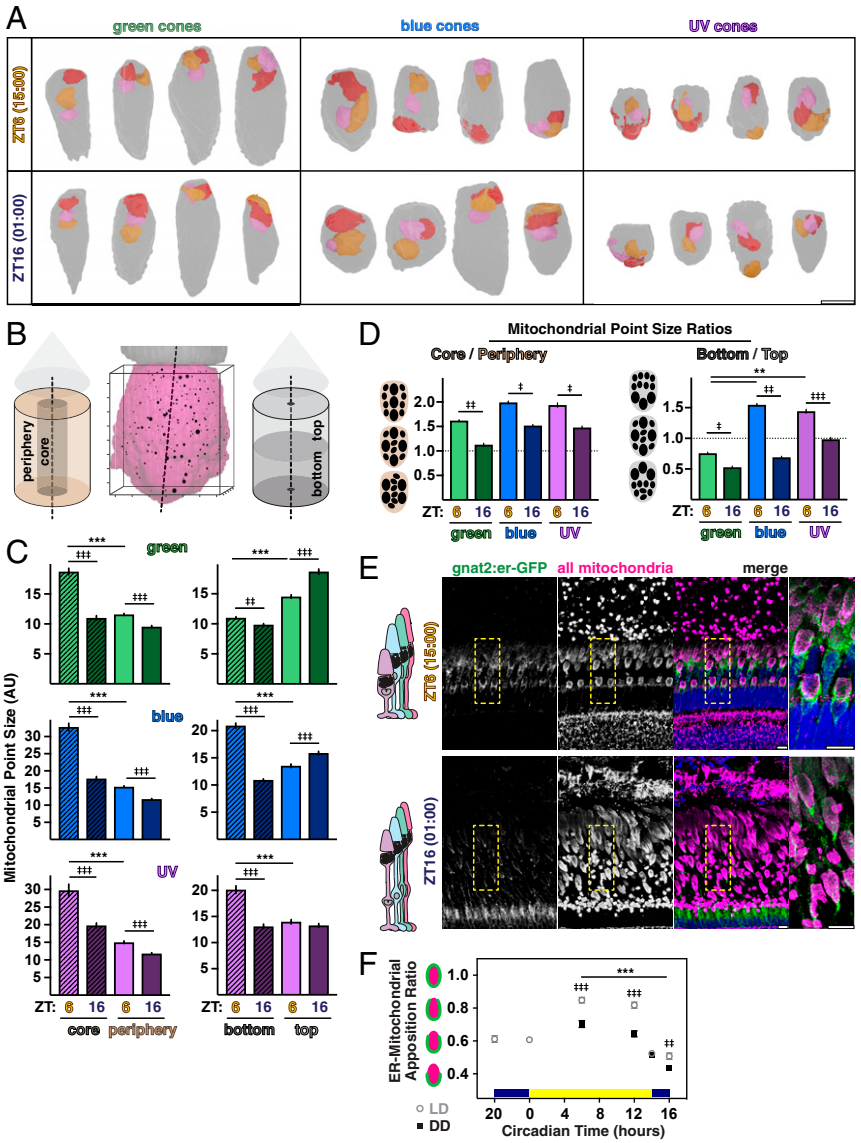

Fig. 3. Distribution of mitochondrial size across the cluster changes throughout the day. (*A*) Three-dimensional renderings of the three largest mitochondria in manually segmented cones at ZT6 and ZT16. OSs are oriented toward the top; ellipsoids, gray. Largest mitochondrion, red; middle, orange and smallest, pink. (Scale bar, 5 μm.) (*B*) Three-dimensional rendering of cone ellipsoid (magenta) and OS (gray) overlaid with the corresponding point cloud. Individual mitochondria are represented at their X-Y-Z locations; point size corresponds to relative mitochondrial size. Points were separated into core and peripheral or top and bottom populations. Axis ticks, 1 μm. (*C*) Quantification of mean mitochondrial point size in regions of the cluster for cone subtypes at ZT6 and ZT16. (*D*) Mitochondrial point size ratios quantifying regional core–periphery and bottom–top distributions of mitochondrial size reported in *C* for cone subtypes at ZT6 and ZT16. In *C* and *D*, ‡$P < 0.05$; **$P < 0.01$; ‡‡$P < 0.001$; ***,‡‡‡$P < 0.0001$. (*E*) IHC images of transgenic zebrafish outer retina expressing cone-targeted er-GFP (green) overlaid with mitochondrial and nuclear stains (magenta and blue, respectively) at ZT6 and ZT16. Yellow boxes, zoomed-in areas. (Scale bars, 10 μm.) (*F*) Quantification of mean ER–mitochondrial apposition in blue and UV cones from IHC for LD or DD groups. ‡‡$P < 0.01$. ***,‡‡‡$P < 0.0001$. *SI Appendix*, Table S2 lists statistical information and Ns from all groups.

and three different mitochondrial respiratory chain markers (Fig. 4*G*, yellow arrowheads). The structures are feasibly the size of a single mitochondrion (0.5- to 1-μm length), contain both cone mito-cpYFP and respiratory proteins, and lie between the cluster and the nucleus. They were present only at overnight timepoints ZT16 and ZT20, and in multiple animals over two generations. While we could not unequivocally identify these structures in SBFSEM, mitochondrial trafficking may occur between the cluster and cell body prior to light onset.

Mitochondria Share Material and Extrude It from the Cell in Darkness. In nearly all cones, we found dark deposits inside and between mitochondria throughout the day in SBFSEM images (Fig. 5 *A*, *Top*). Similar deposits are present in published EM images of cone mitochondrial clusters in other zebrafish (figure 2 of ref. 16), walleye (figures 5 and 7 of ref. 49), frogs (figure 2 of ref. 50), pigeons (figure 16 of ref. 51), shrews (figures 2, 7, and 10 of ref. 52), and ground squirrels (figure 5 of ref. 17), as well as mice and albino zebrafish (*SI Appendix*, Figs. S3 and S5, yellow arrowheads). When manually segmented and 3D rendered, we found these electron-dense lamellar whorls can span several micrometers, contacting the matrices of multiple mitochondria and/or the OS (Fig. 5 *A*, *Bottom*). Most deposits lie inside of single mitochondria, but they appear in the cytosol and occasionally cross the plasma membrane (Fig. 5 *B*, *Top*). This apparent extrusion most often

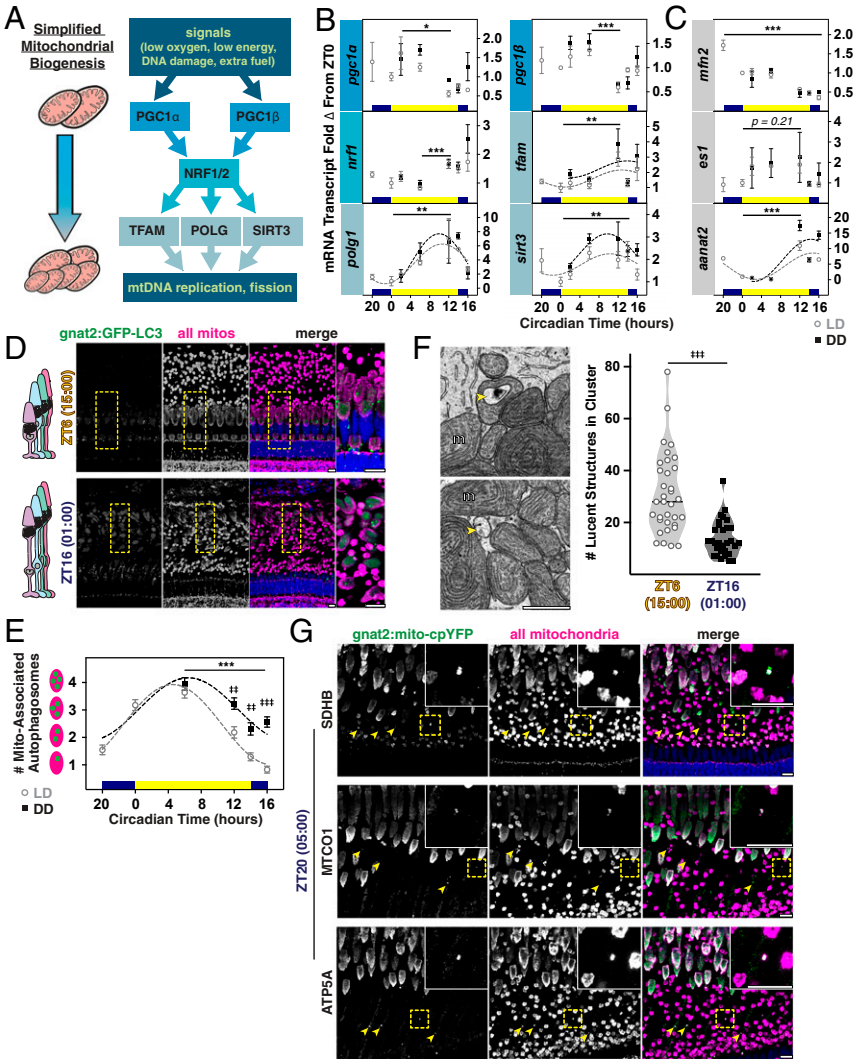

Fig. 4. Mitogenesis genes peak in the evening, when fewer autophagosomes associate with mitochondrial clusters. (*A*) Simplified pathway for mitogenesis. (*B* and *C*) Quantification of mRNA transcripts from whole retinas measured using qPCR: in *B*, six mitogenesis genes, and in *C*, the mitochondrial fusion factor *mfn2*, the mitochondrial enlargement factor *es1*, and a control gene *aanat2*. LD, open circles; DD, black squares. $*P < 0.05$. $**P < 0.01$. $***P < 0.0001$. (*D*) IHC images of transgenic zebrafish outer retina expressing cone-targeted GFP-LC3 (green) overlaid with mitochondrial and nuclear stains (magenta and blue, respectively) at ZT6 and ZT16. Yellow boxes, zoomed-in areas. (Scale bars, 10 μm.) (*E*) Quantification of mitochondrial LC3-positive puncta in blue and UV cones from IHC for LD or DD groups. $‡‡P < 0.001$. $***,‡‡‡P < 0.0001$. (*F*, *Left*) SEM images of lucent autophagosomal structures (yellow arrowheads) inside and between cone mitochondria (m). (Scale bar, 1 μm.) (*F*, *Right*) Violin plots quantifying lucent structures in clusters at ZT6 (empty circles) and ZT16 (black squares); lines represent median. $‡‡‡P < 0.0001$. (*G*) IHC images of transgenic cone-targeted mito-cpYFP (green) counterstained for SDHB, MTCO1, or ATP5A (magenta) and nuclei (blue) at 05:00 (ZT20). Yellow arrowheads and *Insets* indicate mislocalized mitochondria. (Scale bars, 10 μm.) *SI Appendix*, Table S2 lists statistical information and Ns from all groups.

occurs as single events, but some cells displayed multiple concurrent exit sites (Fig. 5 *B*, *Bottom*).

Other neurons can eject mitochondrial material via nanotunnel-like extensions (47). Three-dimensional analysis revealed that in cones, extruded material either remains near the cell surface or forms stalks that can reach 5 μm, terminating in diffuse lamellar extracellular sacs (Fig. 5 *C*, *Top* and Movie S3). The stalks appear as 40- to 90-nm electron-dense rings surrounding a hollow core. In the extracellular space stalks and sacs can connect, creating networks that link discrete populations of mitochondria within a cluster (Fig. 5 *C*, *Bottom* and Movie S4). These deposits and their extrusion in darkness were observed in nearly all cones but seldom in rods; in one instance extrusion was observed in two neighboring rods (Fig. 5*D*).

To quantify cone mitochondrial deposits and extrusion events in day and night, we used a ranking system to blindly score clusters imaged with SBFSEM. The presence of mitochondrial deposits is similar between day and night (Fig. 5 *E*, *Left*). However, extrusion events occur almost exclusively at night, and most cells had multiple events (Fig. 5 *E*, *Right*). While the composition of the deposits is not known, they provide a physical link between cone mitochondria and the interphotoreceptor matrix (IPM).

Mitochondrial Succinate Metabolism Is More Active in Darkness Due to Altered Succinate Dehydrogenase Activity. Mitochondrial metabolism in whole mouse retinas is more active in darkness (3). However, ∼96% of photoreceptors in mouse retinas are rods (53), while zebrafish retinas have ∼50% cones (54, 55). To measure mitochondrial activity in cones, we performed enzyme histochemistry with fresh-frozen retina sections from LD or DD albino zebrafish collected throughout the day. Some albino mouse (56) and zebrafish (57) strains undergo light-induced retinal degeneration, but under

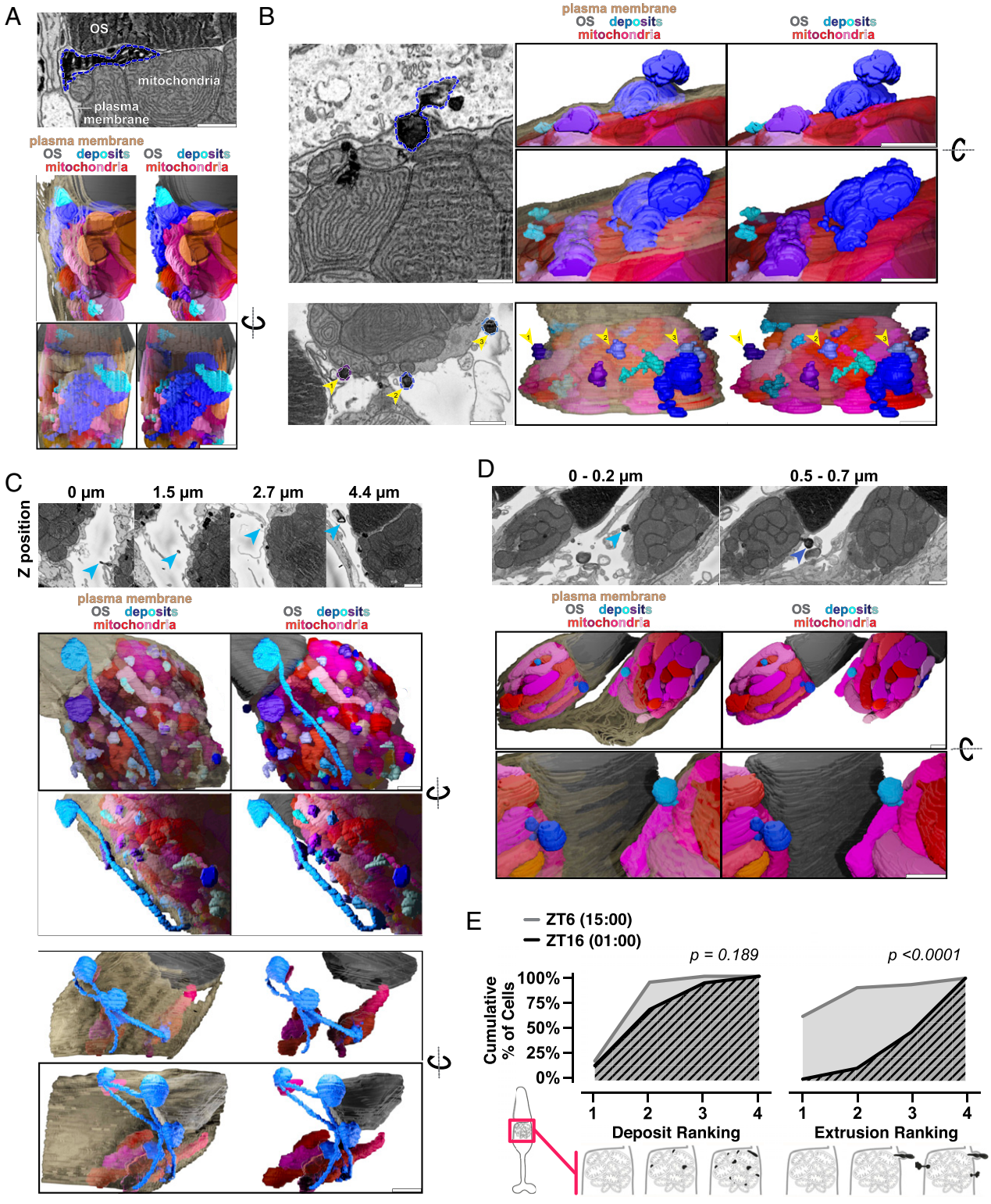

Fig. 5. Mitochondria share material and extrude it from the cell in darkness. (*A*) SBFSEM image (*Top*) of deposits associated with cone mitochondria and corresponding 3D renderings (*Bottom*). One large deposit (blue outline) below the OS is associated with multiple mitochondria. (*B*) SBFSEM images showing extrusion of mitochondrial-associated deposits from cones, with 3D renderings. (*B*, *Top*) Extrusion of one deposit (blue outline). (*B*, *Bottom*) Multiple extrusion events in one cell (blue-violet outlines, yellow arrows). (*C*) SBFSEM images showing stalks and networks in the extracellular space, and corresponding 3D renderings. (*C*, *Middle*) One extruded deposit tethered to mitochondria by a stalk (blue arrows). (*C*, *Bottom*) Branched network of extruded material contacting three distinct populations of cone mitochondria from one cell. (*D*) Extrusion of mitochondrial-associated deposits from two neighboring rods. (*D*, *Top*) SBFSEM minimum intensity projections over 0.2-µm depth highlighting extrusion events (blue arrows). (*D*, *Bottom*) Three-dimensional rendering. (All scale bars, 1 µm.) Beige, plasma membrane; gray, OSs; reds, mitochondria; blues, deposits. (*E*) Quantification of deposits and extrusion events at ZT6 (gray) and ZT16 (black). For deposits: 1 (no mitochondrial deposits) to 4 (every mitochondrion having a deposit). For the number of extrusion events: 1 (no events) to 4 (more than three events). *SI Appendix*, Table S2 lists Ns from all groups.

normal facility lighting our albino zebrafish display healthy central retinal morphology and mitochondrial clusters (*SI Appendix*, Fig. S5). Activities of succinate dehydrogenase (SDH, complex II) and cytochrome *c* oxidase (COX, complex IV) were assayed separately (58); their roles in mitochondrial metabolism are highlighted in Fig. 6*A*. Histochemistry was performed for all timepoints in parallel, and stain intensities of single cones were measured from light microscopy images (Fig. 6*B*).

While COX activity remains robust and stable throughout the day, SDH activity in cones increases 25 to 30% in darkness (Fig. 6*C*). SDH activity in the DD group is elevated at all times of day, suggesting possible repression of SDH activity by light in cones. Additionally SDH activity appears primarily in red-green double cones, compared to strong COX activity observed in all cone subtypes, rods, and the inner retina (Fig. 6*B*, arrowheads).

As validation, we used metabolite labeling coupled with gas chromatography mass spectroscopy (GC/MS) to assay activity of SDH in light- or dark-adapted zebrafish retinas around ZT6. Whole retinas were incubated with U-^{13}C labeled succinate (dark green boxes, Fig. 6*A*), which SDH converts to U-^{13}C fumarate; fumarate is readily interconverted to malate via the enzyme fumarase (59). Labeled fumarate and malate accumulate faster in dark-adapted retinas (Fig. 6*D*). A 2.75-fold higher initial rate of formation for both fumarate and malate (Fig. 6*E*) is consistent with higher SDH activity in darkness observed using histochemistry. To determine if succinate uptake was altered in darkness, we assayed labeled metabolites in media after 60 min, but did not find significantly lower amounts of labeled succinate (Fig. 6*F*). Fig. 6*G* depicts steady-state metabolite labeling in retinas and media after 60 min in light or darkness; succinate levels are similar in light and dark, but metabolites downstream of SDH accumulate in the media.

Discussion

Comparisons of Cone Mitochondria between Species and Cone Subtypes. In zebrafish cones, hundreds of heterogeneous mitochondria pack between the nucleus and OS (16). In this report we quantified mitochondrial number, size, complexity, and 3D distribution in zebrafish cone subtypes. Compared with mouse cones (60) (*SI Appendix*, Fig. S3), zebrafish cone mitochondria are more numerous, smaller, and densely packed, with elaborate cristae patterning (61). The dense packing and disparate mitochondrial volumes between cone subtypes may reflect nutrient and oxygen access in the avascular zebrafish retina (20); double cones closer to the RPE and blood supply could fuel more mitochondria. These spatial constraints, the high SDH activity we observed in double cones, and previous studies showing unique metabolic activity in short-wavelength cones (62, 63) suggest that diverse metabolic strategies support cone subtypes.

Half the animals in our SBFSEM study had larger green cone mitochondrial clusters than the others; the same retinal area was imaged for all animals and single cones did not display this feature. Retinomotor movements occur in cone subtypes at slightly different times (26), so our timepoints may have captured intermediate states for green cones. Alternately, zebrafish green cones may exist as multiple subtypes. Blue and UV cones in zebrafish each express one form of the light-sensitive protein opsin; green cones express four opsins across the adult retina (64, 65), but single-cell analysis is needed to determine if green cone subtypes exist.

Mitochondrial Size in Photoreceptors. Mitochondrial size is linked to energetic output; in other cells smaller mitochondria respire less (4, 66). However, in zebrafish cones small, morphologically simple mitochondria may contribute more toward energy production. Zebrafish single cone mitochondria are smaller and simpler at night, when energy demands and mitochondrial respiration are likely highest. Small mitochondria in cones populate the cluster periphery, closest to oxygen and fuels. Cristae in these small mitochondria generally display the organized, linear structure linked to higher energetic output (61).

Like other species (51, 67) zebrafish cones form megamitochondria, maintained by the enlargement factor ES1 (31, 42). We did not detect changes to *es1* mRNA transcripts in whole retinas, but observed juxtaposed megamitochondria in all cones throughout the day. The biological role of megamitochondria is unknown, but their densely packed cristae suggest roles beyond canonical respiration (68). Membrane lipids concentrated in megamitochondrial cristae can form a conduit for oxygen (69, 70). Many cone megamitochondria exhibit a central body with projections extending toward the cluster periphery; these projections toward the ER could be a site for mitogenesis (67). Further, cone megamitochondria (30, 52) and mitochondrial-derived ellipsosomes (71, 72) in other species guide light toward the OS. Zebrafish visual sensitivity is regulated by light and the circadian clock (73), so daily mitochondrial rearrangements may contribute to vision.

Mitochondrial Turnover in Photoreceptors. Maintenance of healthy mitochondria and mtDNA is crucial, particularly in the retina. mtDNA mutations (13) and disrupted autophagy (74) are associated with retinal degeneration, and aging human cones accumulate mtDNA mutations and mitochondrial abnormalities (19, 75). In some forms of age-related macular degeneration, cone mitochondrial clusters remodel and mitochondria translocate toward the nucleus (12).

Genes required for mitogenesis (38) undergo circadian changes in retinal expression in a manner that supports mitogenesis at night onset, although it is unknown which retinal cell(s) this occurs in. At ER–mitochondrial contact sites the ER stimulates mitophagy (76) by recruiting autophagic machinery (77) and initiating mitochondrial fission (34). In single cones, ER concentrates around the cluster during the day, when clusters contain more autophagosomes and fewer mitochondria. Together this suggests that cones undergo daily mitochondrial turnover involving ER.

SDH Activity and Potential Regulation in the Retina. Fewer mitochondria during the day could result in the reduced cone SDH activity we detected using histochemistry. Zebrafish cones have higher SDH activity than other retinal cells, consistent with studies of human (58, 75) and salamander retinas (78). Cone SDH activity increases at night, when regulation from the zebrafish circadian clock (23, 79) could promote mitochondrial succinate uptake (80). However, we did not find evidence of increased succinate uptake in darkness, and frozen sections used for histochemistry don't require transporters for substrate uptake. Thus, our observations of cone SDH activity likely resulted from changes to expression or posttranslational modifications, rather than succinate availability.

Light (81, 82) and time of day (83, 84) can affect SDH expression in other cells. Additionally, SDH can be regulated by competitive inhibition (85, 86), phosphorylation (87, 88), acetylation (89), and succinylation (90). mRNA transcripts for the mitochondrial deacetylase SIRT3 increase in retinas prior to night onset, but regulation of SDH by SIRT3 in retinas has not been explored. In photoreceptors, both SIRT3 and the mitochondrial desuccinylase SIRT5 are necessary for normal function (91). Further, cristae structure can influence respiration (8, 92), in part by driving SDH supercomplexation (93). SDH catalyzes a reversible reaction in mouse retinas (94); we used succinate to quantify forward capacity of SDH.

Mitochondrial Deposits in Photoreceptors. In photoreceptors, whorled deposits contact the matrices of multiple mitochondria. The deposits are distinct from melanosomes; they are present in albino zebrafish photoreceptors. We did not investigate their composition, but they resemble osmiophilic structures observed in and around mitochondria of other cells, proposed to have roles in lipid metabolism (figure 8 of ref. 95 and figure 4 of ref. 96), mitochondrial

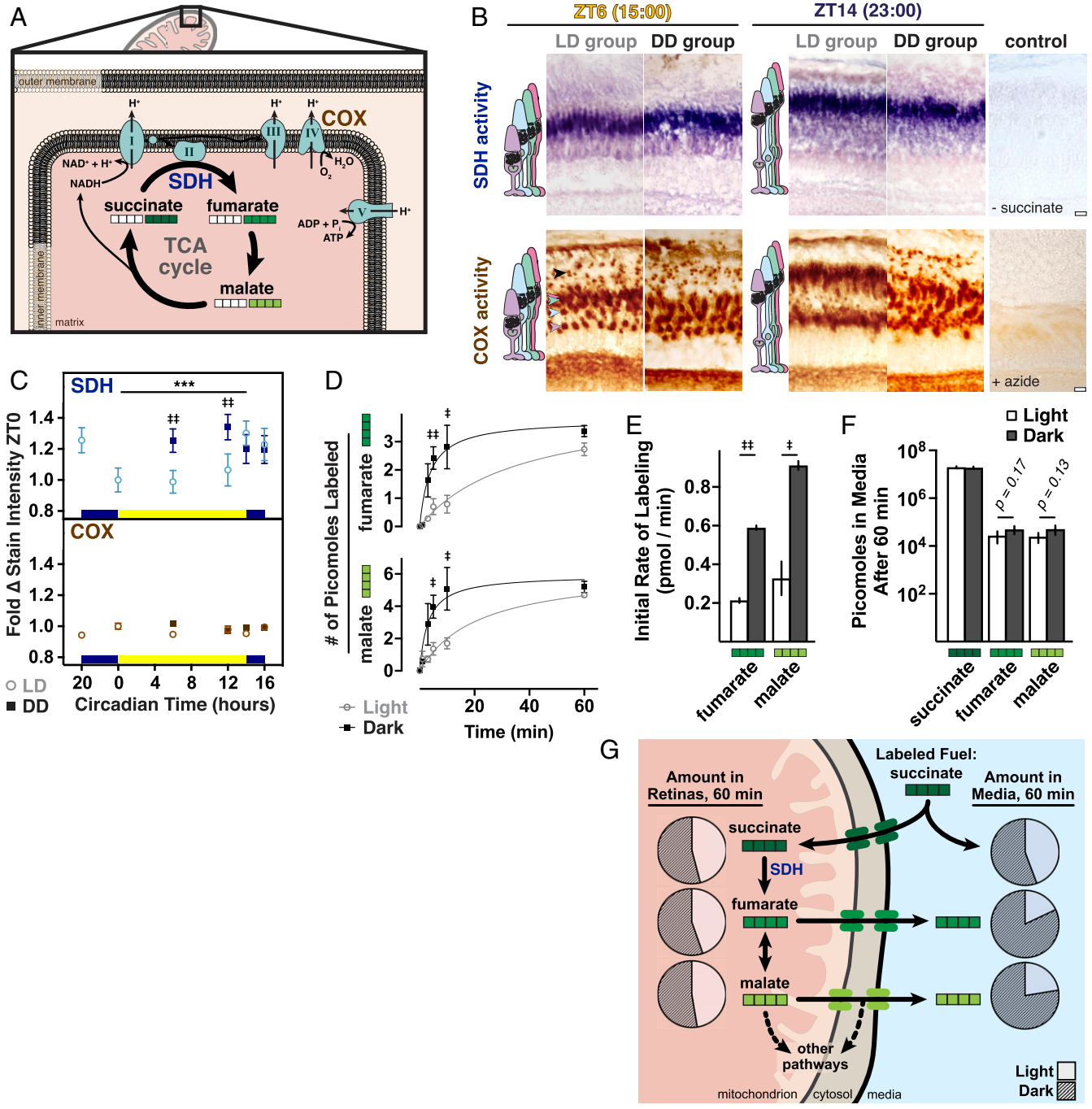

Fig. 6. Mitochondrial metabolism is more active in darkness due to altered SDH activity. (*A*) Schematic of SDH in the tricarboxylic acid (TCA) cycle and electron transport chain, including COX also assayed in *B*. White squares represent ^{12}C carbons; green squares, ^{13}C carbons for labeling experiments (*D–F*). (*B*) Light microscopy images of histochemical staining for SDH (blue) and COX (brown) activities. Shown are frozen sections from albino zebrafish at ZT6 and ZT14 (23:00) from LD and DD groups. Negative controls lacked substrate or contained an inhibitor. Arrowheads indicate corresponding cone subtype and rod (black) mitochondrial clusters. (Scale bars, 10 μm.) (*C*) Quantification of mean SDH and COX stain intensities in single clusters from LD (open circles) or DD (dark squares) groups; data normalized to ZT0. ‡‡$P < 0.001$. ***$P < 0.0001$. (*D*) Mean incorporation of ^{13}C label from U-^{13}C succinate into fumarate and malate. Whole retinas from light- or dark-adapted zebrafish were incubated in U-^{13}C succinate in light or dark; ^{13}C incorporation was determined with GC/MS. (*E*) Initial rates of formation of fumarate and malate from U-^{13}C succinate in light and dark from the first 5 min of incubation. In *D* and *E*, ‡$P < 0.05$; ‡‡$P < 0.001$. (*F*) Amounts of U-^{13}C-labeled succinate, fumarate, and malate in media after 60-min light or dark incubation with retinas in U-^{13}C succinate. *SI Appendix*, Table S2 lists *P* values and Ns from all groups. (*G*) Schematic of steady-state metabolites inside and outside of retinas after 60-min incubation with labeled succinate. Pie charts denote relative amounts of metabolites in light (unfilled areas) and dark (filled areas).

degradation (97, 98), and peroxisome synthesis (99). Further, ER stacks can encircle mitochondria, forming a lamellar structure to initiate mitophagy (77). Collectively this suggests that photoreceptor mitochondrial deposits may mediate lipid homeostasis and/or mitochondrial clearance.

Nightly Extrusion of Mitochondrial Material. Mitochondrial deposits are extruded from cones at night. The events we report are morphologically distinct from photoreceptor endocytosis (100, 101), exocytosis (102, 103), and from published examples of mitochondrial extrusion in other cells (104–108). Unlike these events, extrusion of

cone mitochondrial deposits shows no evidence of fusion with the plasma membrane, and the released material remains associated with the cell surface and underlying mitochondria.

The extruded material can connect to the extracellular space via thin stalks that terminate in diffuse lamellar sacs. Neurons have been reported to release and tether mitochondrial material (47, 48) via thin stalks ∼200 nm wide and terminal multivesiculate sacs of ∼3-μm diameter. The extracellular structures attached to photoreceptors are smaller (∼60-nm stalks and ∼1-μm sacs), and sacs do not contain vesicles. The stalks are smaller than tunneling nanotubes (109), which can transport mitochondria (110–112). Photoreceptors can exchange proteins via an unknown mechanism (113), but we did not observe connections between cones. The extracellular structures could link cones to the IPM, a scaffold of carbohydrates and bound proteins (114, 115) where cones occupy a distinct metabolic microenvironment (116, 117). At night the zebrafish outer retina becomes disorganized by retinomotor movements, so the extracellular structures could physically anchor cones to the IPM.

In summary, we report a quantitative analysis of daily mitochondrial dynamics in cone photoreceptors. At night, when energy demands are likely highest, a mitogenesis event in retinas precedes increases in cone metabolic activity and the number of small mitochondria in single cones. During the day, mitochondrial number decreases, perhaps mediated by fusion and/or mitophagy. We also report a dense lamellar material that is shared between mitochondria and extrudes from the cell at night, sometimes forming extracellular networks. These daily changes to cone mitochondria can support energy production at night, regulated by light and the circadian clock. This study did not include phototransduction mutants or lengthy dark adaptation; differences we report between LD and DD groups could be attributed to effects of light masking and/or master circadian rhythms (118, 119). Elucidating the makeup of mitochondrial deposits, regulation of SDH, role of ER–mitochondrial contacts, and rates and locations of mitochondrial turnover in healthy cones will contribute to an understanding of how mitochondrial abnormalities in aging and disease affect vision.

Materials and Methods

Zebrafish Maintenance and Retina Collection. Research was authorized by the University of Washington Institutional Animal Care and Use Committee. Wild-type, transgenic, and albino adult zebrafish were maintained on a 14-h/10-h light/dark cycle. Twenty-four hours prior to experiments, fish were fasted in either continuous darkness (DD) or standard room light (LD). See *SI Appendix* for details about fish lines and sample collection.

Serial Block-Face Scanning Electron Microscopy. Wild-type or albino zebrafish eyes were fixed and prepared in resin blocks as described previously (18). Serial sections were cut at 50-nm thickness and imaged in the outer retina, 100 to 200 μm from the optic nerve. Z-stack images were processed and measured using the TrakEM2 plugin for ImageJ (research resource identifier [RRID]:SCR_008954). See *SI Appendix* for details about sample preparation and image analysis.

Immunohistochemistry. Albino or transgenic zebrafish eyes were fixed, cryosectioned, stained, and confocal imaged as described previously (41). Z-stacks from each timepoint were blindly analyzed using ImageJ (RRID:SCR_002285). *SI Appendix*, Table S1 lists antibodies and stains; see *SI Appendix* for details about sample preparation and image analysis.

Quantitative PCR. RNA was extracted from wild-type zebrafish eyes, reverse transcribed into cDNA, and analyzed using qPCR as described in *SI Appendix*. Primer sequences are reported in *SI Appendix*, Table S3. Cosinor curves fitted to each dataset were used to determine circadian rhythmicity according to cutoff values (more than twofold change and $P < 0.05$ from ANOVA analysis) (120); data meeting this cutoff display dashed lines. *SI Appendix*, Table S4 lists fitting parameters and statistics.

Enzyme Histochemistry. Histochemical enzyme activity was assayed similarly to previous studies in human (58) and mouse retina (121). Briefly, albino zebrafish eyes were dissected, frozen in optimal cutting temperature compound and cryosectioned for parallel staining. SDH and COX activity stain solutions were applied for 10 min at 37 °C, then washed, mounted, and imaged with a light microscope. Stain intensity of single cones was blindly quantified using ImageJ. See *SI Appendix* for details about sample preparation and image analysis.

Isotopic ^{13}C Succinate Labeling and Mass Spectrometry. Light- or dark-adapted wild-type zebrafish eyes were dissected and incubated in 1 mM D-[U-^{13}C]-succinate with 1 mM unlabeled glucose for the specified timepoints, then washed in phosphate buffered saline and flash frozen in liquid nitrogen. Metabolites were extracted from retinas, derivatized, and analyzed using GC/MS. See *SI Appendix* for details about sample collection and metabolite analysis.

Data Analysis. Data were processed using Microsoft Excel (RRID:SCR_016137); statistical tests were performed using GraphPad Prism (RRID:SCR_002798). *SI Appendix*, Table S2 lists experimental numbers (Ns) and statistical analysis methods for each figure. The 3D renderings and animations from SBFSEM were created using Blender (RRID:SCR_008606) (122).

Data Availability. Single cell data from IHC, SBFSEM, histochemistry, succinate labeling data have been deposited in Open Science Framework (https://osf.io/qaed8).

ACKNOWLEDGMENTS. Funding for this work was provided by the University of Washington (UW) Art and Rita Levinson undergraduate research scholarship (D.C.B.), NIH NEI 5T32-EY007031 (M.M.G. and K.M.R.), NIH NEI R01-EY026020 (S.E.B.), NIH NEI R01-EY06641 (J.B.H.), NIH NIA T32-AG000057 (K.A.T.), and UW Vision Core grant NIH NEI P30-EY001730 (to Maureen Neitz). We thank Amandeep Dhami, Ashlee Evans, Carson Adams, Stephanie Sloat, and Alexey Merz for help with data analysis and thoughtful discussion; Stan Kim provided zebrafish care at the UW Institute for Stem Cell and Regenerative Medicine Aquatics Center.

1. H. Okawa, A. P. Sampath, S. B. Laughlin, G. L. Fain, ATP consumption by mammalian rod photoreceptors in darkness and in light. *Curr. Biol.* **18**, 1917–1921 (2008).
2. M. M. LaVail, Rod outer segment disk shedding in rat retina: Relationship to cyclic lighting. *Science* **194**, 1071–1074 (1976).
3. J. Du *et al.*, Phototransduction influences metabolic flux and nucleotide metabolism in mouse retina. *J. Biol. Chem.* **291**, 4698–4710 (2016).
4. H. Chen, A. Chomyn, D. C. Chan, Disruption of fusion results in mitochondrial heterogeneity and dysfunction. *J. Biol. Chem.* **280**, 26185–26192 (2005).
5. P. de Goede, J. Wefers, E. C. Brombacher, P. Schrauwen, A. Kalsbeek, Circadian rhythms in mitochondrial respiration. *J. Mol. Endocrinol.* **60**, R115–R130 (2018).
6. V. S. Van Laar *et al.*, Evidence for compartmentalized axonal mitochondrial biogenesis: Mitochondrial DNA replication increases in distal axons as an early response to Parkinson's disease-relevant stress. *J. Neurosci.* **38**, 7505–7515 (2018).
7. C. K. E. Bleck, Y. Kim, T. B. Willingham, B. Glancy, Subcellular connectomic analyses of energy networks in striated muscle. *Nat. Commun.* **9**, 5111 (2018).
8. S. Cogliati, J. A. Enriquez, L. Scorrano, Mitochondrial cristae: Where beauty meets functionality. *Trends Biochem. Sci.* **41**, 261–273 (2016).
9. Y. C. Wong, W. Peng, D. Krainc, Lysosomal regulation of inter-mitochondrial contact fate and motility in charcot-marie-tooth type 2. *Dev. Cell* **50**, 339–354.e4 (2019).
10. D. Cieri, M. Brini, T. Calì, Emerging (and converging) pathways in Parkinson's disease: Keeping mitochondrial wellness. *Biochem. Biophys. Res. Commun.* **483**, 1020–1030 (2017).
11. H. Chen, D. C. Chan, Mitochondrial dynamics–Fusion, fission, movement, and mitophagy–In neurodegenerative diseases. *Hum. Mol. Genet.* **18**, R169–R176 (2009).
12. K. M. Litts, J. D. Messinger, K. B. Freund, Y. Zhang, C. A. Curcio, Inner segment remodeling and mitochondrial translocation in cone photoreceptors in age-related macular degeneration with outer retinal tubulation. *Invest. Ophthalmol. Vis. Sci.* **56**, 2243–2253 (2015).
13. E. Lefevere *et al.*, Mitochondrial dysfunction underlying outer retinal diseases. *Mitochondrion* **36**, 66–76 (2017).
14. A. Ames 3rd, Y. Y. Li, E. C. Heher, C. R. Kimble, Energy metabolism of rabbit retina as related to function: High cost of Na^+ transport. *J. Neurosci.* **12**, 840–853 (1992).
15. B. S. Winkler, Glycolytic and oxidative metabolism in relation to retinal function. *J. Gen. Physiol.* **77**, 667–692 (1981).
16. R. Tarboush, I. Novales Flamarique, G. B. Chapman, V. P. Connaughton, Variability in mitochondria of zebrafish photoreceptor ellipsoids. *Vis. Neurosci.* **31**, 11–23 (2014).
17. B. S. Sajdak *et al.*, Evaluating seasonal changes of cone photoreceptor structure in the 13-lined ground squirrel. *Vision Res.* **158**, 90–99 (2019).

18. M. A. Kanow *et al*., Biochemical adaptations of the retina and retinal pigment epithelium support a metabolic ecosystem in the vertebrate eye. *eLife* **6**, e28899 (2017).
19. T. C. Nag, S. Wadhwa, Immunolocalisation pattern of complex I-V in ageing human retina: Correlation with mitochondrial ultrastructure. *Mitochondrion* **31**, 20–32 (2016).
20. J. Stone, D. van Driel, K. Valter, S. Rees, J. Provis, The locations of mitochondria in mammalian photoreceptors: Relation to retinal vasculature. *Brain Res.* **1189**, 58–69 (2008).
21. A. Bentmann *et al*., Divergent distribution in vascular and avascular mammalian retinae links neuroglobin to cellular respiration. *J. Biol. Chem.* **280**, 20660–20665 (2005).
22. J. Y.-A. Chang, L. Shi, M. L. Ko, G. Y. P. Ko, Circadian regulation of mitochondrial dynamics in retinal photoreceptors. *J. Biol. Rhythms* **33**, 151–165 (2018).
23. G. M. Cahill, Clock mechanisms in zebrafish. *Cell Tissue Res.* **309**, 27–34 (2002).
24. G. Vatine, D. Vallone, Y. Gothilf, N. S. Foulkes, It's time to swim! Zebrafish and the circadian clock. *FEBS Lett.* **585**, 1485–1494 (2011).
25. P. A. Raymond, L. K. Barthel, G. A. Curran, Developmental patterning of rod and cone photoreceptors in embryonic zebrafish. *J. Comp. Neurol.* **359**, 537–550 (1995).
26. G. J. Menger, J. R. Koke, G. M. Cahill, Diurnal and circadian retinomotor movements in zebrafish. *Vis. Neurosci.* **22**, 203–209 (2005).
27. C. Hodel, S. C. F. Neuhauss, O. Biehlmaier, Time course and development of light adaptation processes in the outer zebrafish retina. *Anat. Rec. A Discov. Mol. Cell. Evol. Biol.* **288**, 653–662 (2006).
28. M. M. Giarmarco, W. M. Cleghorn, S. R. Sloat, J. B. Hurley, S. E. Brockerhoff, Mitochondria maintain distinct Ca^{2+} pools in cone photoreceptors. *J. Neurosci.* **37**, 2061–2072 (2017).
29. A. E. Vincent *et al*., Quantitative 3D mapping of the human skeletal muscle mitochondrial network. *Cell Rep.* **26**, 996–1009.e4 (2019).
30. W. Knabe, S. Skatchkov, H. J. Kuhn, "Lens mitochondria" in the retinal cones of the tree-shrew Tupaia belangeri. *Vision Res.* **37**, 267–271 (1997).
31. S. Utsumi *et al*., Presence of ES1 homolog in the mitochondrial intermembrane space of porcine retinal cells. *Biochem. Biophys. Res. Commun.* **524**, 542–548 (2020).
32. L. P. Tyrrell *et al*., A novel cellular structure in the retina of insectivorous birds. *Sci. Rep.* **9**, 15230 (2019).
33. J. Kim *et al*., The presence of megamitochondria in the ellipsoid of photoreceptor inner segment of the zebrafish retina. *Anat. Histol. Embryol.* **34**, 339–342 (2005).
34. J. R. Friedman *et al*., ER tubules mark sites of mitochondrial division. *Science* **334**, 358–362 (2011).
35. F. Korobova, V. Ramabhadran, H. N. Higgs, An actin-dependent step in mitochondrial fission mediated by the ER-associated formin INF2. *Science* **339**, 464–467 (2013).
36. M. Amiri, P. J. Hollenbeck, Mitochondrial biogenesis in the axons of vertebrate peripheral neurons. *Dev. Neurobiol.* **68**, 1348–1361 (2008).
37. A. A. George *et al*., Synaptojanin 1 is required for endolysosomal trafficking of synaptic proteins in cone photoreceptor inner segments. *PLoS One* **9**, e84394 (2014).
38. R. C. Scarpulla, R. B. Vega, D. P. Kelly, Transcriptional integration of mitochondrial biogenesis. *Trends Endocrinol. Metab.* **23**, 459–466 (2012).
39. C. Ploumi, I. Daskalaki, N. Tavernarakis, Mitochondrial biogenesis and clearance: A balancing act. *FEBS J.* **284**, 183–195 (2017).
40. L. Artuso *et al*., Mitochondrial DNA metabolism in early development of zebrafish (Danio rerio). *Biochim. Biophys. Acta* **1817**, 1002–1011 (2012).
41. R. A. Hutto *et al*., Increasing Ca^{2+} in photoreceptor mitochondria alters metabolites, accelerates photoresponse recovery, and reveals adaptations to mitochondrial stress. *Cell Death Differ.* **27**, 1067–1085 (2020).
42. T. Masuda, Y. Wada, S. Kawamura, ES1 is a mitochondrial enlarging factor contributing to form mega-mitochondria in zebrafish cones. *Sci. Rep.* **6**, 22360 (2016).
43. M. Wang, Z. Zhong, Y. Zhong, W. Zhang, H. Wang, The zebrafish period2 protein positively regulates the circadian clock through mediation of retinoic acid receptor (RAR)-related orphan receptor α (Rorα). *J. Biol. Chem.* **290**, 4367–4382 (2015).
44. R. J. Youle, D. P. Narendra, Mechanisms of mitophagy. *Nat. Rev. Mol. Cell Biol.* **12**, 9–14 (2011).
45. F. Strappazzon *et al*., AMBRA1 is able to induce mitophagy via LC3 binding, regardless of PARKIN and p62/SQSTM1. *Cell Death Differ.* **22**, 419–432 (2015).
46. S. Kawajiri *et al*., PINK1 is recruited to mitochondria with parkin and associates with LC3 in mitophagy. *FEBS Lett.* **584**, 1073–1079 (2010).
47. I. Melentijevic *et al*., C. elegans neurons jettison protein aggregates and mitochondria under neurotoxic stress. *Nature* **542**, 367–371 (2017).
48. C.-H. O. Davis *et al*., Transcellular degradation of axonal mitochondria. *Proc. Natl. Acad. Sci. U.S.A.* **111**, 9633–9638 (2014).
49. M. M. Januschka, D. A. Burkhardt, S. L. Erlandsen, R. L. Purple, The ultrastructure of cones in the walleye retina. *Vision Res.* **27**, 327–341 (1987).
50. A. M. Mercurio, E. Holtzman, Smooth endoplasmic reticulum and other agranular reticulum in frog retinal photoreceptors. *J. Neurocytol.* **11**, 263–293 (1982).
51. T. Ishikawa, E. Yamada, Atypical mitochondria in the ellipsoid of the photoreceptor cells of vertebrate retinas. *Invest. Ophthalmol.* **8**, 302–316 (1969).
52. S. Lluch, M. J. López-Fuster, J. Ventura, Giant mitochondria in the retina cone inner segments of shrews of genus Sorex (Insectivora, Soricidae). *Anat. Rec. A Discov. Mol. Cell. Evol. Biol.* **272**, 484–490 (2003).
53. Y. Tsukamoto, K. Morigiwa, M. Ueda, P. Sterling, Microcircuits for night vision in mouse retina. *J. Neurosci.* **21**, 8616–8623 (2001).
54. P. A. Raymond *et al*., Patterning the cone mosaic array in zebrafish retina requires specification of ultraviolet-sensitive cones. *PLoS One* **9**, e85325 (2014).
55. K. D. Larison, R. Bremiller, Early onset of phenotype and cell patterning in the embryonic zebrafish retina. *Development* **109**, 567–576 (1990).
56. M. M. LaVail, G. M. Gorrin, M. A. Repaci, L. A. Thomas, H. M. Ginsberg, Genetic regulation of light damage to photoreceptors. *Invest. Ophthalmol. Vis. Sci.* **28**, 1043–1048 (1987).
57. T. S. Vihtelic, C. J. Doro, D. R. Hyde, Cloning and characterization of six zebrafish photoreceptor opsin cDNAs and immunolocalization of their corresponding proteins. *Vis. Neurosci.* **16**, 571–585 (1999).
58. R. M. Andrews, P. G. Griffiths, M. A. Johnson, D. M. Turnbull, Histochemical localisation of mitochondrial enzyme activity in human optic nerve and retina. *Br. J. Ophthalmol.* **83**, 231–235 (1999).
59. B. Andersen, Lack of deviation from Michaelis–Menten kinetics for pig heart fumarase. *Biochem. J.* **189**, 653–654 (1980).
60. S. Sloat *et al*., Quantification of mitochondrial structure in photoreceptors. *Invest. Ophthalmol. Vis. Sci.* **57**, 566 (2016).
61. G. A. Perkins, M. H. Ellisman, D. A. Fox, Three-dimensional analysis of mouse rod and cone mitochondrial cristae architecture: Bioenergetic and functional implications. *Mol. Vis.* **9**, 60–73 (2003).
62. J. H. Kam *et al*., Mitochondrial absorption of short wavelength light drives primate blue retinal cones into glycolysis which may increase their pace of aging. *Vis. Neurosci.* **36**, E007 (2019).
63. T. M. Nork, S. A. McCormick, G. M. Chao, J. V. Odom, Distribution of carbonic anhydrase among human photoreceptors. *Invest. Ophthalmol. Vis. Sci.* **31**, 1451–1458 (1990).
64. A. Chinen, T. Hamaoka, Y. Yamada, S. Kawamura, Gene duplication and spectral diversification of cone visual pigments of zebrafish. *Genetics* **163**, 663–675 (2003).
65. M. Takechi, S. Kawamura, Temporal and spatial changes in the expression pattern of multiple red and green subtype opsin genes during zebrafish development. *J. Exp. Biol.* **208**, 1337–1345 (2005).
66. M. Maryanovich *et al*., An MTCH2 pathway repressing mitochondria metabolism regulates haematopoietic stem cell fate. *Nat. Commun.* **6**, 7901 (2015).
67. W. Knabe, H. J. Kuhn, Morphogenesis of megamitochondria in the retinal cone inner segments of Tupaia belangeri (Scandentia). *Cell Tissue Res.* **285**, 1–9 (1996).
68. D. B. Slautterback, Mitochondria in cardiac muscle cells of the canary and some other birds. *J. Cell Biol.* **24**, 1–21 (1965).
69. N. Desaulniers, T. S. Moerland, B. D. Sidell, High lipid content enhances the rate of oxygen diffusion through fish skeletal muscle. *Am. J. Physiol.* **271**, R42–R47 (1996).
70. M. R. Urschel, K. M. O'Brien, High mitochondrial densities in the hearts of Antarctic icefishes are maintained by an increase in mitochondrial size rather than mitochondrial biogenesis. *J. Exp. Biol.* **211**, 2638–2646 (2008).
71. E. F. MacNichol Jr, Y. W. Kunz, J. S. Levine, F. I. Hárosi, B. A. Collins, Ellipsosomes: Organelles containing a cytochrome-like pigment in the retinal cones of certain fishes. *Science* **200**, 549–552 (1978).
72. T. C. Nag, J. Bhattacharjee, Retinal ellipsosomes: Morphology, development, identification, and comparison with oil droplets. *Cell Tissue Res.* **279**, 633–637 (1995).
73. L. Li, J. E. Dowling, Zebrafish visual sensitivity is regulated by a circadian clock. *Vis. Neurosci.* **15**, 851–857 (1998).
74. N. Rodríguez-Muela *et al*., Lysosomal membrane permeabilization and autophagy blockade contribute to photoreceptor cell death in a mouse model of retinitis pigmentosa. *Cell Death Differ.* **22**, 476–487 (2015).
75. M. J. Barron *et al*., Mitochondrial abnormalities in ageing macular photoreceptors. *Invest. Ophthalmol. Vis. Sci.* **42**, 3016–3022 (2001).
76. M. Hamasaki *et al*., Autophagosomes form at ER-mitochondria contact sites. *Nature* **495**, 389–393 (2013).
77. Y. Huang *et al*., A "Lamellar structure" contributes to autophagosome biogenesis and mitophagy in zebrafish hepatocytes. *Fish Shellfish Immunol.* **81**, 83–91 (2018).
78. C. L. Moore, E. R. Guberg, The distribution of succinic semialdehyde dehydrogenase in the brain and retina of the tiger salamander. *Brain Res.* **67**, 467–478 (1974).
79. P. Li *et al*., CLOCK is required for maintaining the circadian rhythms of Opsin mRNA expression in photoreceptor cells. *J. Biol. Chem.* **283**, 31673–31678 (2008).
80. T. Cai *et al*., The circadian protein CLOCK regulates cell metabolism via the mitochondrial carrier SLC25A10. *Biochim. Biophys. Acta Mol. Cell Res.* **1866**, 1310–1321 (2019).
81. V. N. Popov, A. T. Eprintsev, D. N. Fedorin, A. U. Igamberdiev, Succinate dehydrogenase in Arabidopsis thaliana is regulated by light via phytochrome A. *FEBS Lett.* **584**, 199–202 (2010).
82. F. K. Gu, L. Chen, B. Ni, X. M. Zhang, A comparative study on the electron microscopic enzymo-cytochemistry of Paramecium bursaria from light and dark cultures. *Eur. J. Protistol.* **38**, 267–278 (2002).
83. H. Akimoto, T. Kinumi, Y. Ohmiya, Circadian rhythm of a TCA cycle enzyme is apparently regulated at the translational level in the dinoflagellate Lingulodinium polyedrum. *J. Biol. Rhythms* **20**, 479–489 (2005).
84. A. B. Reddy *et al*., Circadian orchestration of the hepatic proteome. *Curr. Biol.* **16**, 1107–1115 (2006).
85. B. A. Ackrell, E. B. Kearney, M. Mayr, Role 3f oxalacetate in the regulation of mammalian succinate dehydrogenase. *J. Biol. Chem.* **249**, 2021–2027 (1974).
86. V. R. Potter, K. P. Dubois, Studies on the mechanism of hydrogen transport in animal tissues: VI. Inhibitor studies with succinic dehydrogenase. *J. Gen. Physiol.* **26**, 391–404 (1943).
87. R. Acín-Pérez *et al*., ROS-triggered phosphorylation of complex II by Fgr kinase regulates cellular adaptation to fuel use. *Cell Metab.* **19**, 1020–1033 (2014).
88. A. K. Nath *et al*., PTPMT1 inhibition lowers glucose through succinate dehydrogenase phosphorylation. *Cell Rep.* **10**, 694–701 (2015).
89. H. Cimen *et al*., Regulation of succinate dehydrogenase activity by SIRT3 in mammalian mitochondria. *Biochemistry* **49**, 304–311 (2010).
90. J. Park *et al*., SIRT5-mediated lysine desuccinylation impacts diverse metabolic pathways. *Mol. Cell* **50**, 919–930 (2013).

91. J. B. Lin *et al*., NAMPT-mediated NAD(+) biosynthesis is essential for vision in mice. *Cell Rep.* **17**, 69–85 (2016).
92. R. Guo, J. Gu, S. Zong, M. Wu, M. Yang, Structure and mechanism of mitochondrial electron transport chain. *Biomed. J.* **41**, 9–20 (2018).
93. F. Liu, P. Lössl, B. M. Rabbitts, R. S. Balaban, A. J. R. Heck, The interactome of intact mitochondria by cross-linking mass spectrometry provides evidence for coexisting respiratory supercomplexes. *Mol. Cell. Proteomics* **17**, 216–232 (2018).
94. C. M. Bisbach *et al*., Succinate can shuttle reducing power from the hypoxic retina to the O_2-rich pigment epithelium. *Cell Rep.* **31**, 107606 (2020).
95. E. J. Blanchette-Mackie, R. O. Scow, Movement of lipolytic products to mitochondria in brown adipose tissue of young rats: An electron microscope study. *J. Lipid Res.* **24**, 229–244 (1983).
96. D. M. Tarlow *et al*., Lipogenesis and the synthesis and secretion of very low density lipoprotein by avian liver cells in nonproliferating monolayer culture. Hormonal effects. *J. Cell Biol.* **73**, 332–353 (1977).
97. V. Soubannier *et al*., A vesicular transport pathway shuttles cargo from mitochondria to lysosomes. *Curr. Biol.* **22**, 135–141 (2012).
98. A. Sugiura, G. L. McLelland, E. A. Fon, H. M. McBride, A new pathway for mitochondrial quality control: Mitochondrial-derived vesicles. *EMBO J.* **33**, 2142–2156 (2014).
99. A. Sugiura, S. Mattie, J. Prudent, H. M. McBride, Newly born peroxisomes are a hybrid of mitochondrial and ER-derived pre-peroxisomes. *Nature* **542**, 251–254 (2017).
100. J. G. Hollyfield, H. H. Varner, M. E. Rayborn, G. I. Liou, C. D. Bridges, Endocytosis and degradation of interstitial retinol-binding protein: Differential capabilities of cells that border the interphotoreceptor matrix. *J. Cell Biol.* **100**, 1676–1681 (1985).
101. J. G. Hollyfield, M. E. Rayborn, Endocytosis in the inner segment of rod photoreceptors: Analysis of Xenopus laevis retinas using horseradish peroxidase. *Exp. Eye Res.* **45**, 703–719 (1987).
102. R. Rea *et al*., Streamlined synaptic vesicle cycle in cone photoreceptor terminals. *Neuron* **41**, 755–766 (2004).
103. X. Wen, G. W. Saltzgaber, W. B. Thoreson, Kiss-and-run is a significant contributor to synaptic exocytosis and endocytosis in photoreceptors. *Front. Cell. Neurosci.* **11**, 286 (2017).
104. O. Gasko, D. Danon, Deterioration and disappearance of mitochondria during reticulocyte maturation. *Exp. Cell Res.* **75**, 159–169 (1972).
105. C. F. Simpson, J. M. Kling, The mechanism of mitochondrial extrusion from phenylhydrazine-induced reticulocytes in the circulating blood. *J. Cell Biol.* **36**, 103–109 (1968).
106. K. Unuma, T. Aki, T. Funakoshi, K. Hashimoto, K. Uemura, Extrusion of mitochondrial contents from lipopolysaccharide-stimulated cells: Involvement of autophagy. *Autophagy* **11**, 1520–1536 (2015).
107. K. G. Lyamzaev *et al*., Novel mechanism of elimination of malfunctioning mitochondria (mitoptosis): Formation of mitoptotic bodies and extrusion of mitochondrial material from the cell. *Biochim. Biophys. Acta* **1777**, 817–825 (2008).
108. C. Géminard, A. de Gassart, M. Vidal, Reticulocyte maturation: Mitoptosis and exosome release. *Biocell* **26**, 205–215 (2002).
109. H.-H. Gerdes, R. N. Carvalho, Intercellular transfer mediated by tunneling nanotubes. *Curr. Opin. Cell Biol.* **20**, 470–475 (2008).
110. J. Lu *et al*., Tunneling nanotubes promote intercellular mitochondria transfer followed by increased invasiveness in bladder cancer cells. *Oncotarget* **8**, 15539–15552 (2017).
111. X. Wang, H.-H. Gerdes, Transfer of mitochondria via tunneling nanotubes rescues apoptotic PC12 cells. *Cell Death Differ.* **22**, 1181–1191 (2015).
112. A. Sartori-Rupp *et al*., Correlative cryo-electron microscopy reveals the structure of TNTs in neuronal cells. *Nat. Commun.* **10**, 342 (2019).
113. A. Ortin-Martinez *et al*., A reinterpretation of cell transplantation: GFP transfer from donor to host photoreceptors. *Stem Cells* **35**, 932–939 (2017).
114. M. Ishikawa, Y. Sawada, T. Yoshitomi, Structure and function of the interphotoreceptor matrix surrounding retinal photoreceptor cells. *Exp. Eye Res.* **133**, 3–18 (2015).
115. J. G. Hollyfield, Hyaluronan and the functional organization of the interphotoreceptor matrix. *Invest. Ophthalmol. Vis. Sci.* **40**, 2767–2769 (1999).
116. A. J. Adler, R. E. Southwick, Distribution of glucose and lactate in the interphotoreceptor matrix. *Ophthalmic Res.* **24**, 243–252 (1992).
117. L. V. Johnson, G. S. Hageman, J. C. Blanks, Interphotoreceptor matrix domains ensheath vertebrate cone photoreceptor cells. *Invest. Ophthalmol. Vis. Sci.* **27**, 129–135 (1986).
118. N. Mrosovsky, R. G. Foster, P. A. Salmon, Thresholds for masking responses to light in three strains of retinally degenerate mice. *J. Comp. Physiol. A Neuroethol. Sens. Neural Behav. Physiol.* **184**, 423–428 (1999).
119. C. M. Altimus *et al*., Rod photoreceptors drive circadian photoentrainment across a wide range of light intensities. *Nat. Neurosci.* **13**, 1107–1112 (2010).
120. C. DeVera, G. Tosini, Circadian analysis of the mouse retinal pigment epithelium transcriptome. *Exp. Eye Res.* **193**, 107988 (2020).
121. Y. Chinchore, T. Begaj, D. Wu, E. Drokhlyansky, C. L. Cepko, Glycolytic reliance promotes anabolism in photoreceptors. *eLife* **6**, e25946 (2017).
122. M. M. Giarmarco *et al*, Giarmarco_PNAS_2020_rawdata. Open Science Framework. https://osf.io/qaed8. Deposited 7 October 2020.